International Journal of Hydrogen Energy 112 (2025) 347–353

Contents lists available at ScienceDirect

International Journal of Hydrogen Energy

journal homepage: www.elsevier.com/locate/he

A novel approach for estimating hydrogen uptake and diffusion coefficient

Luca Gritti *, Denny Coffetti, Marina Cabrini, Tommaso Pastore

Department of Engineering Applied Science, University of Bergamo, Italy

ARTICLE INFO

Handling Editor: Dr M Djukic

Keywords:
Diffusion coefficient
hydrogen uptake
Simulation model
Electrochemical charging
Alkaline environments
Pipeline steel

ABSTRACT

Hydrogen diffusional parameters in metallic alloys were evaluated for API 5L-grade X65 steel by introducing a simplified approach using a single-compartment electrochemical cell. The experimental hydrogen flow from electrochemically pre-charged specimens is interpolated through a numerical approach, with a simulated target curve derived for a specific geometry. The diffusion coefficient and concentration of diffusible hydrogen were estimated after hydrogen charging in alkaline solutions at different levels of cathodic polarisation. The results show constant and reproducible values of diffusivity despite the level of polarisation, and the concentration of diffusible hydrogen increases with cathodic overpotential, depending on the composition of the solution.

1. Introduction

Currently, several approaches are considered through extensive experimental research to evaluate the hydrogen compatibility pure and in mixing with other gases [1,2] and hydrogen embrittlement susceptibility [3,4] of metal alloys. Hydrogen-induced brittle fracture is associated with diffusible hydrogen, as described in several studies [5–9] if associated in slow strain and plastic deformation [10–15]. There are various approaches to investigating the diffusion coefficient and hydrogen uptake, such as thermal desorption spectroscopy [16–18], melt extraction, vacuum extraction [19], silver micro-printing [20], tritium autoradiography, gas chromatography [21] and electrochemistry impedance spectroscopy [22]. An important strategy to evaluate the hydrogen uptake and diffusion coefficient is using electrochemical methods based on a Devanathan–Stachurski permeation cell [23,24]. These methods use an electrochemical double compartment with a thin plate between the two semi-cells. One side is used to charge the sample through cathodic polarisation, while the other side is anodically polarised, thus maintaining the hydrogen concentration on a surface that is equal to zero. Therefore, diffusible hydrogen flux passes from one side to another. It is possible to estimate the diffusion coefficient following different approaches, such as based on the elapsed time (t_{lag}), the breakthrough time or the slope method [25].

A new simplified approach to estimate the solubility and diffusion coefficient using a single-compartment cell has been introduced [26]. This methodology involves a two-step procedure, with an initial phase of electrochemistry charging to saturate the metallic sample through cathodic polarisation at potentials below the equilibrium potential for hydrogen evolution, followed by a subsequent phase of discharging under anodic polarisation at potentials above the equilibrium potential. The time evolution of the anodic current during the discharging phase is affected by the flux of diffusible hydrogen egressing from the sample. The latter depends on the initial concentration of diffusible hydrogen in the material (e.g. the diffusible hydrogen uptake) by the diffusion coefficient and the elapsed time between the end of the charging step and the start of discharging. An approach to estimate the diffusion coefficient and hydrogen concentration with this methodology measuring the current transient by anodic/cathodic pulse polarisation applied, it is deriving the parameters via analytical solution [27,28]. Usually, it needs to impose one-dimensional flow experimental conditions, because all analyses and models, even complex ones that consider e.g. trapping effect, involve well-defined and oriented one-dimensional flows.

This study examined a three-dimensional flux of hydrogen to estimate of diffusible hydrogen content and diffusion coefficient in an API 5L-grade X65 pipeline steel. These parameters were evaluated using a single-compartment electrochemical cell on steel specimens pre-charged in different alkaline solutions and cathodic polarisations to obtain different levels of hydrogen saturation. The diffusion coefficient and diffusible hydrogen concentration in the metal were obtained by fitting the experimental discharging current density through a normalised desorption curve derived for the specific geometry of the specimens using a three-dimensional FEM model (Finite Element Method).

* Corresponding author.
E-mail address: uca.gritti1@unibg.it (L. Gritti).

https://doi.org/10.1016/j.ijhydene.2025.02.400
Received 1 October 2024; Received in revised form 11 February 2025; Accepted 25 February 2025
Available online 1 March 2025

2. Experimental

2.1. Materials and solutions

The test was performed on cylindrical specimens of high-strength low-alloy (HSLA) API 5L-grade X65 steel, with a diameter of 13 mm and a height of 45 mm, obtained from a 14 mm thick hot-rolled, longitudinally welded pipe for gas and oil transport, with a ferritic–pearlitic banded microstructure. The chemical composition of steel is reported in Table 1. On top of the cylinder, an M3 thread was used to fix the specimen to the sample holder, which consisted of a threaded rod. Only a couple of threads were used to change the initial geometry as little as possible. For all analyses, all samples were processed with papers up to 1200 grit and degreased with acetone.

Two alkaline test solutions were considered: a 26.5 g/l of Na_2CO_3 + 42 g/l of $NaHCO_3$ carbonate–bicarbonate solution of pH 10, previously adopted to simulate soil water in studies on stress corrosion cracking [29], and a 0.1 M sodium hydroxide solution.

2.2. Experimental Lay-out

The electrochemical single-compartment cell is shown in Fig. 1. The sample was positioned at the centre of the cell to ensure uniform current distribution from the counter-electrode. It was connected to the working electrode via a threaded rod, which was insulated by a glass tube. An activated titanium mesh basket was used as the counter-electrode. The potential was measured using a saturated calomel electrode (SCE) reference electrode with a lugging probe. The cell was filled with the test solution, which was maintained at a constant room temperature of approximately 23 ± 0.1 °C using a thermostatic bath. Prior to the experiment, the solutions were deaerated for 12 h through nitrogen bubbling and maintained during the entire testing time.

2.3. Experimental procedure

The experimental procedure was conducted in different phases. Initially, after sample assembly and nitrogen flushing, the test cell was filled with the deaerated solution. The specimens were then polarised at +0.306 V versus SCE to obtain the passivation curve. The passivation potential was assumed to be equal to that recommended by the ISO17081 standard for the detection side of the Devanathan–Stachurski cell operating in the 0.1 M sodium hydroxide solution expressed versus SCE. This potential was also applied to the tests conducted in the carbonate–bicarbonate solution at pH 10. As confirmed by the potentiodynamic test in Fig. 2, this value was within the passivity range of steel for this environment.

Hydrogen charging was conducted through potentiostatic cathodic polarisation in the range of −1 to −1.8 V versus SCE for 15 h, which was sufficient time for the specimens to achieve a homogeneous hydrogen concentration at a typical value of diffusivity reported for low-carbon steel [30,31]. During this step, part of the hydrogen produced on the surface was absorbed into the steel. At the end of the charging phase, polarisation was immediately inverted to apply the anodic polarisation again at +0.306 V versus SCE for 15 h to measure the discharging current curve. The discharging anodic current represents the passivity current enhanced by the current due to the oxidation of hydrogen egressing from the metal. To estimate the net current due to hydrogen oxidation, the experimental value of the discharging current was depurated by subtracting the passivation current curve measured during the early phase. The integration of the net hydrogen current over the testing

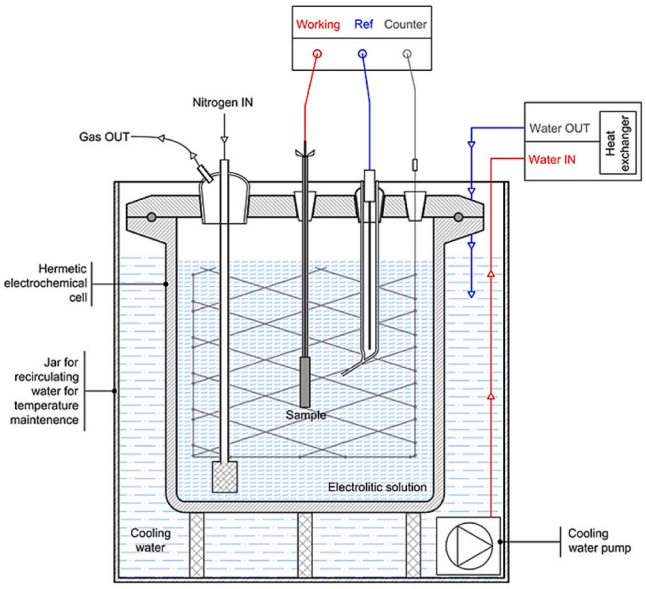

Fig. 1. Scheme of the electrochemical charging/discharging cell with a single compartment.

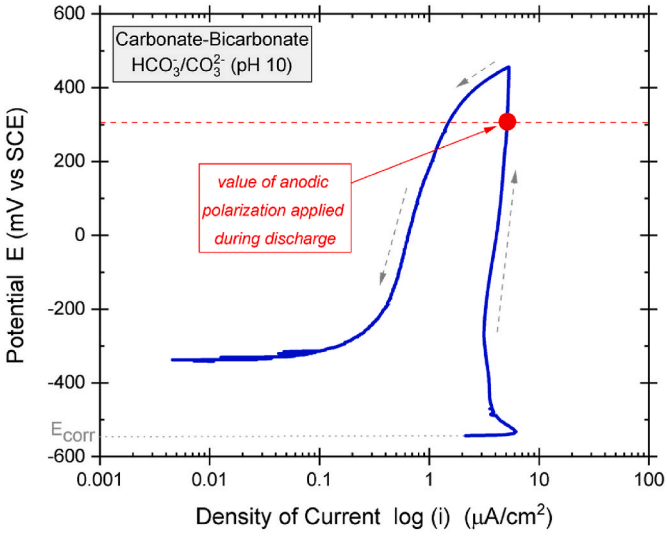

Fig. 2. Forward and reverse potentiodynamic polarisation curve in a deaerated solution of carbonate–bicarbonates (pH 10). This test was executed at room temperature with a scan rate of 10 mV/min from −0.2 to +500 mv vs. OCP.

time allows for the estimation of the charge $Q_{Hadj}(t)$ due to the oxidation of diffusible hydrogen mass egress from the sample. Finally, the mass of hydrogen outgoing ($M_{Hadj}(t)$) from the sample can be derived using Faraday's law.

The residual mass of hydrogen that remains in the sample $M_{res}(t)$ is given by the following relation:

$$M_{res}(t) = M_{\infty} - M_{Hadj}(t) \tag{2.1}$$

where M_{∞} is the steady-state value of the outgoing mass discharge of

Table 1
Composition of material HSLA X65 grade.

Elem.	C	Mn	Si	P	S	Nb	Mo	V	Cu	Ni	Cr	Ceq
[%WT]	0.09	1.64	0.24	0.003	0.002	0.049	0.002	<0.0000	0.011	0.017	0.031	**0.366**

hydrogen. The average concentration of residual diffusible hydrogen that remains in the sample $C_{res}(t)$ at time t can then be evaluated by dividing the residual mass of hydrogen by the sample mass (M_{sample}), as shown in (2.2)

$$C_{res}(t) = \frac{M_{res}(t)}{M_{sample}} \cdot 10^6 \quad [ppm] \tag{2.2}$$

3. Theory and calculation: FEM simulation

To simulate electrochemical discharge correctly, it was necessary to model the actual geometry of the specimen used during experimental tests in similar discharging conditions. Thus, tri-dimensional diffusion of hydrogen from the sample during electrochemical discharge was simulated through the FEM model using *COMSOL Multiphysics* in cylindrical coordinates. The specific cylinder geometry of the sample adopted in this work was considered. The diffusion process in the metal is described by Fick's second law (3.1), where C and t are the hydrogen concentration and time, respectively.

$$\begin{cases} \dfrac{\partial C}{\partial t} - D\nabla^2 C = 0 \\ \left.\begin{matrix} C_0^* = constant \\ D = constant \end{matrix}\right] \quad I.C \\ C_s = 0 \;\; on\; surfaces] \quad B.C \end{cases} \tag{3.1}$$

The model includes the initial conditions (*I.C.*) of homogeneous hydrogen concentration C_0^* and constant diffusion coefficient D. During discharging, the boundary condition (*B.C.*) on the metal–solution surface imposes the concentration C_s to be equal to zero. This condition describes the behaviour of anodic polarisation imposed during electrochemical discharging on the specimen. In fact, during discharge the atomic hydrogen in the lattice that spread up to the surface it is immediately sequestered on the surface. This due to the hydrogen atoms can react with further discharging H^+ ions producing hydrogen molecules and leave the surface for alkaline environment [32]; therefore it is possible to consider the superficial hydrogen concentration equal to zero. The simulations conducted varying diffusion coefficients D between $1{\cdot}10^{-12}$ and $1{\cdot}10^{-9}\frac{m^2}{s}$ and initial concentrations C_0^* between 0.3 and 10 *ppm*. The flux of hydrogen leaving all sample surfaces is then obtained using Fick's first law (3.2), given the concentration gradient normal to the external sample surface.

$$\phi^*_{egress} = -D{\cdot}\nabla C \tag{3.2}$$

The mole of egress hydrogen ($n^*_{egress}(t)$) was obtained through the integration of the flux over time. Thus, to obtain the average residual concentration (C^*_{res}) that remains in the sample at a certain time, considering an initial concentration C_0^* at the end of charging, the following evaluation is necessary:

$$C^*_{res}(t) = \sum_{t=0}^{\infty} \frac{n^*_{egress}(t=\infty) - n^*_{egress}(t)}{Volume} \quad \left[\frac{mol}{m^3}\right] \tag{3.3}$$

4. Results and discussion

4.1. Elaboration of FEM simulations

Fig. 3 shows the distribution of the hydrogen concentration inside the cylinder sample, modelled at $1{\cdot}10^{-12}\frac{m^2}{s}$ diffusivity, 2 $\frac{mol}{m^3}$ initial homogenous concentration with superficial concentration equal to 0 *ppm* as B.C, after $3{\cdot}10^6$ s. To discretise the geometry, it was used the axial symmetric property of the problem thus it was built a grid mesh only on a single rectangular section with side coinciding with the axis of the cylinder. The mesh is automatically built via the "quadrilateral mesh generator" that create not strictly only quadratic elements, but in places of the geometry where it judges it as necessary, it could be also create triangular elements. In this case, the plane of studied was composed by 1647 quads. The simulation solves the 2009 grades of freedom, with an integration step equal to 60,000 s. It should be noted that the flux comes from all surfaces.

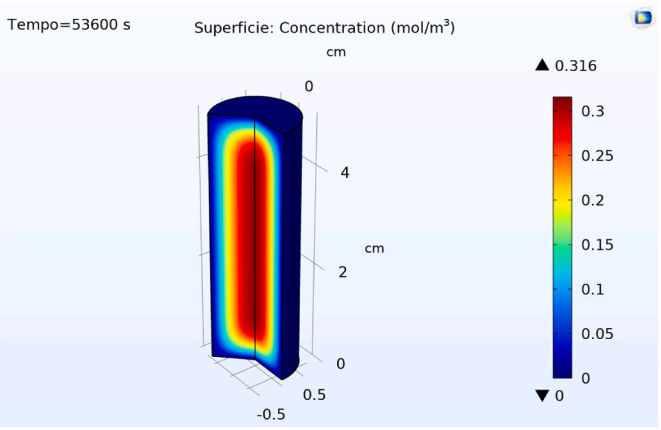

Fig. 3. Simulation result of a cylinder with diameter of 13 mm and a height of 45 mm (the geometry is exactly the experimental ones) of the hydrogen egress to $D = 1{\cdot}10^{-12}\frac{m^2}{s}$ e $C_0^* = 0.347\frac{mol}{m^3}$. The colour map represents the distribution of the hydrogen concentration in $\frac{mol}{m^3}$ after 12440 *s*. It was used 1647 quadrilateral elements. The grade of freedom is 2009, which is used as an integration step equal to 60,000 s. (For interpretation of the references to colour in this figure legend, the reader is referred to the Web version of this article.)

Fig. 4 shows the average concentration of residual hydrogen that remains in the sample (C^*_{res}) that can diffuse during the discharging period estimated via simulations. At the end of all simulations, the flux tended close to zero. Thus, it can be assumed that there is no residual diffusible hydrogen in the metal. Nevertheless, changing the initial concentration of the simulations implies the modification of the initial point of the residual concentration curve, but constant diffusivity guarantees that all branches begin to come closer to zero at the same time. Varying the diffusion coefficient at a constant initial concentration involves large variations of egressing time to achieve a low residual concentration at the end of the simulation. Increasing the diffusion coefficient means having a faster hydrogen outflow and vice versa.

All the simulated curves can be described according to a unique curve (dashed line in Fig. 5) by introducing the dimensionless time $\widehat{T}$ and the dimensionless concentration $\widehat{C}^*(t)$ defined as follows:

$$\widehat{T} = \frac{t{\cdot}D}{r^2} \tag{4.1}$$

$$\widehat{C}^*(t) = \frac{C^*_{res}(t)}{C^*_{res}(t=0)} \equiv \frac{C^*_{res}(t)}{C_0^*} \tag{4.2}$$

where r is the radius of the cylinder. The unique target curve is the result of the overlapping of the first branch of all simulated curves truncated at $\widehat{T} = 0.4$. Investigating the values of the average residual concentration under 1/100 of the initial concentration is not significant because the values are extremely low. Moreover, the first branch of the target curve has the largest amount of hydrogen flux, accounting for the most significant part of interpolating the experimental discharging curves. This curve is independent of the diffusion coefficient and the initial concentration.

4.2. Experimental curves and physically driven optimisation

Fig. 6 shows an example of the experimental curves related to the carbonate–bicarbonate solution. It compares the passivation curve

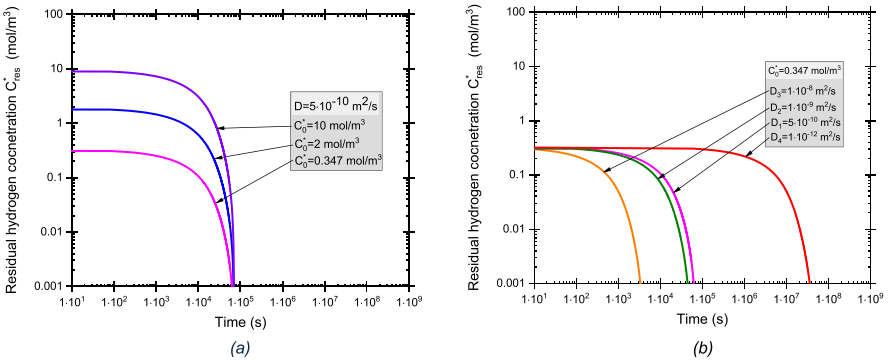

Fig. 4. Simulation curves of the residual average concentration remaining in the sample C^*_{res} vs. discharging time. Curves obtained by different initial concentrations (a) and diffusion coefficients (b).

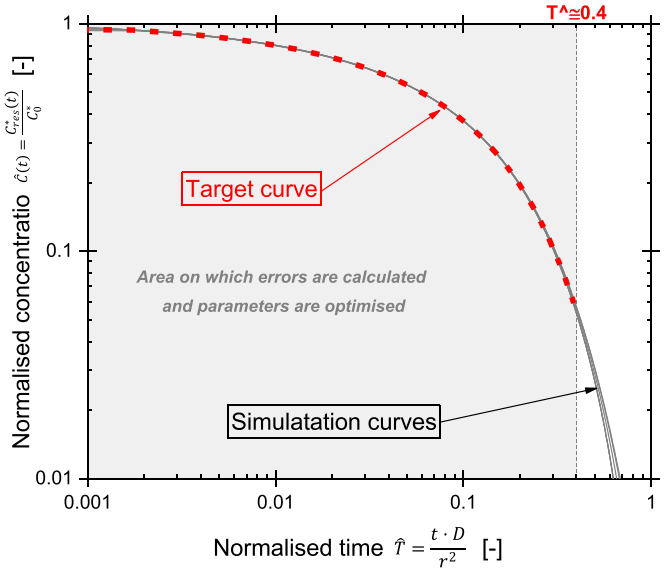

Fig. 5. Target curve obtained from the overlapping of the different normalised simulation curves.

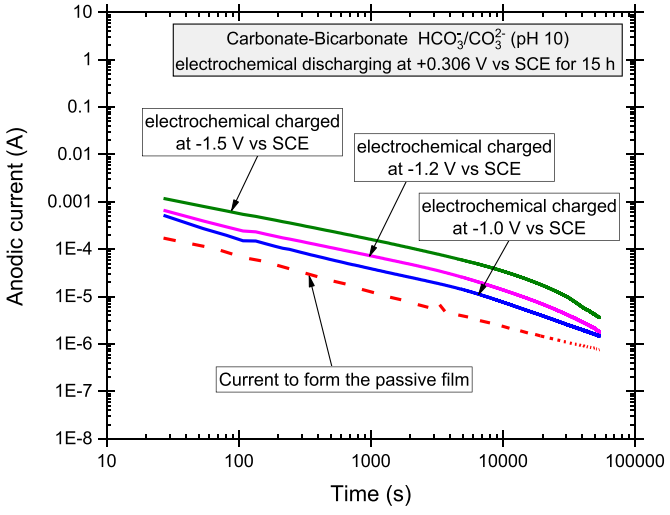

Fig. 6. Comparison between the passivation and discharging curves at +0.306 V vs. SCE of the test in carbonate–bicarbonate solution.

obtained in the early phase with the potentiostatic polarisation discharging at +0.306 V versus SCE after cathodic charging at different potentials. It can be noted that the passivation current is low but not negligible, with respect to the discharge current, even at a high level of hydrogen charging. Thus, it is necessary to depurge the discharging current measured by the passivation contribute, subtracting from discharging curves the passivation curve.

Integrating the net discharging current over time obtains the charge evolution Q_{Hadj} in time. The net charge increases over time due to the egress of hydrogen, and after 15 h of discharge, it achieves a stationarity behaviour (Fig. 7). In fact, 90% of the total charge pass in 8 h. Thus, in the remaining time, the value of the charge pass is very low, and the variation can be assumed to be stationary. Therefore, after 15 h, it is possible to consider that the egress of diffusible hydrogen is complete. The last part of the branch can be assumed to define the stationarity conditions at an infinite time.

The charge trend calculates the mass of the diffusible hydrogen flow through the surface using Equation (2.1), assuming that the last point is stationary. Thus, the curves of the average residual hydrogen concentration $C_{res,adj}(t)$ can be estimated over time using Equation (2.2).

The normalisation approach can be used to estimate the initial hydrogen content C_0 charged, the diffusion coefficient D and the elapsed time t between the end of charging and the initial discharging step through the experimental curves. The experimental data can be normalised in time and concentration using Equations (4.1) and (4.2) by imposing the adequate C_0, D and t_0. In the first attempt, the parameters

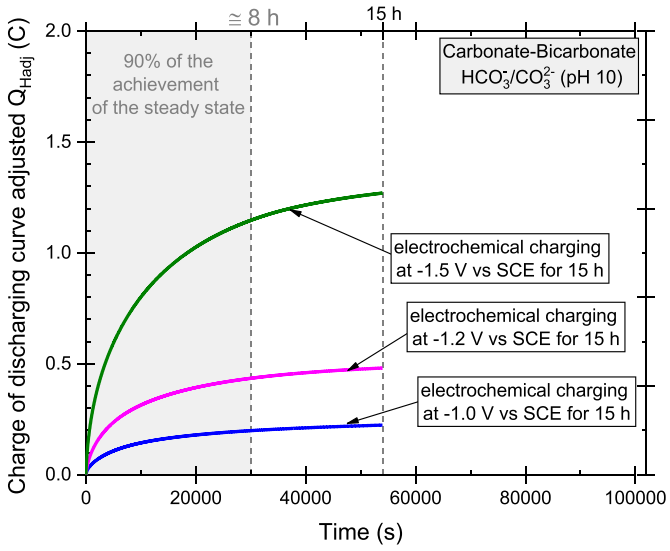

Fig. 7. Charge of the discharging curve at +0.306 V vs. SCE after charging at different cathodic polarisations in carbonate–bicarbonate.

should be evaluated using empirical rules. Thus, it is possible to adapt the normalised experimental data overlapping the unique target curve by changing the parameters C_0, D and t_0 of normalisation. Optimisation minimises the relative error function estimated as the difference between the two above curves. As previously noted, the calculation of the error to optimisation is estimated along the target curve up to the normalised time under 0.4.

This procedure was implemented using a *Matlab Code* and is available on the data in brief [33] and can be downloaded via Mendelay data [34]. This iteration procedure exploits the *fminsearch* function, a nonlinear programming solver that uses the Nelder–Mead simplex. It is a simplex of n+1 points, which are sorted according to the descending value of the function. It discards the worst value and replaces it with a new point according to some criteria.

Fig. 8 illustrates an example of the iteration results for the test in the carbonate–bicarbonate solution with a charging polarisation of −1.5 V versus SCE. The results obtained by interpolation represent the best values of the parameter search D_{opt}, $C_{0,opt}$ and t_0, which allows the matching of the experimental curve with the target curve.

Different cathodic polarisations have been studied, as shown in Fig. 9, for the carbonate–bicarbonate solution. The average residual hydrogen content decreases over time due to sample emptying, and the curves start from an increasingly high concentration with increase the cathodic potential applied. The first experimental value of concentration does not correspond with the true total initial concentration C_0 charged. Part of the hydrogen is lost during polarisation reversal due to the inertia of the electrochemical system and the changing of the pH diffusion layer surrounding the sample. Thus, it is not known when the first atom of hydrogen egresses from the sample, and there is an uncertainty in the initial values of the current (elapsed time t_0). Moreover, it is impossible to estimate the concentration of hydrogen spread into the sample C_0 through the charging curve. This represents the total circulating current during cathodic charge, but it is impossible to quantify the share of the current responsible for the hydrogen chemisorption process. Thus, even if the elapsed time between the end of charging and the start to discharge is close to zero, consistent with the experimental execution, the initial concentration through the physically driven optimisation and the first value of the experimental curve do not coincide perfectly. Nevertheless, if the elapsed time between charge and discharge is negligible, the initial diffusible concentration corresponds approximately to the area under the discharging curve. Thus, it is possible to compare the results obtained through physically driven optimisation ($C_{0,opt}$) by integrating the residual hydrogen concentration curves ($C_{integral}$), as shown in Table 2. The differences are extremely small at about hundredths of ppm.

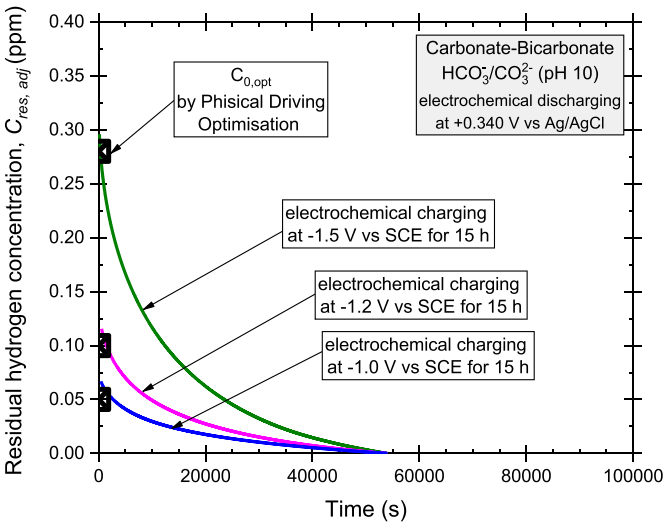

Fig. 9. Residual hydrogen concentration during the discharging step after cathodic charging and hydrogen uptake through physically driven optimisation.

Table 2
Comparison of hydrogen uptake obtained using different methods.

Test Solutions	*Charging Polarisation*	$C_{integral}$ [ppm]	$C_{0,opt}$ [ppm]
Sodium hydroxide 0.1 M	−1.2	0.11	0.08
	−1.5	0.26	0.24
	−1.8	0.25	0.22
Carbonate–bicarbonates 26.5 g/l of Na_2CO_3	−1	0.08	0.05
+ 42 g/l of $NaHCO_3$	−1.2	0.14	0.10
	−1.5	0.31	0.28
	−1.3	0.11	0.09
	−1.5	0.19	0.14
	−2	0.30	0.21
	−1.2	0.06	0.05
	−1.5	0.14	0.11
	−1.8	0.22	0.18

Figs. 10 and 11 show the diffusion coefficients and concentrations estimated by optimisation versus overpotential. This represents the available energy for hydrogen evolution reactions [35]. Overpotential is estimated according to the definition of Equation (4.3), where E is the

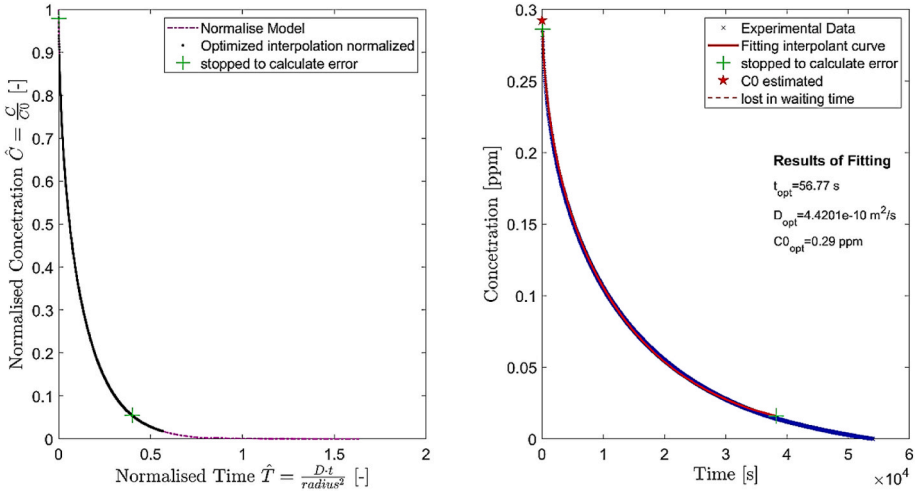

Fig. 8. Estimation of the diffusion coefficient and hydrogen uptake due to the interpolation of the experimental results with the target curve. This test was conducted in the carbonate–bicarbonate solution, with a charging cathodic polarisation of −1.5 V vs. SCE.

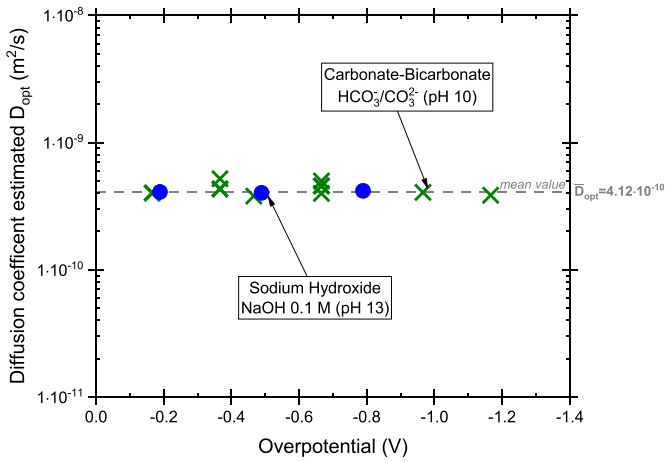

Fig. 10. Optimised diffusion coefficient estimated using the interpolant method for different cathodic overpotentials and several pH values.

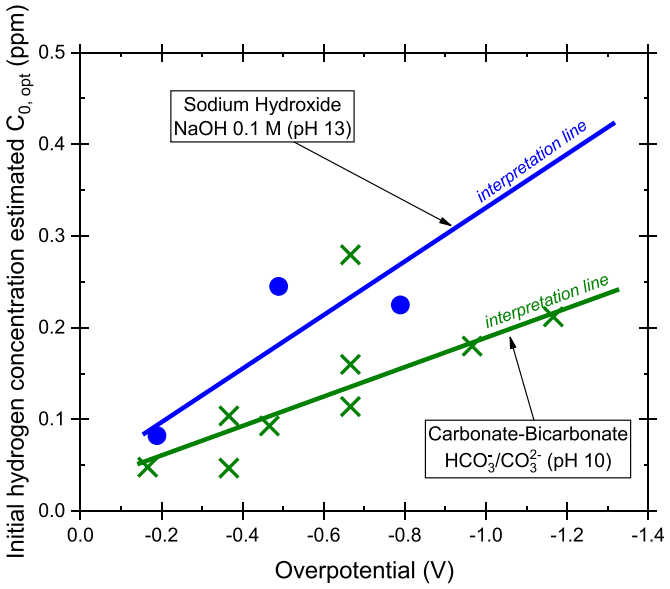

Fig. 11. Initial hydrogen concentration estimated using the interpolant method for different cathodic charging polarisation and several pH values.

potential applied during charging polarisation, and E_{eq} is the equilibrium potential defined by the Nernst equation and is the function of E_0 (standard electrode potential of hydrogen) and pH value of the solution.

$$\eta = |E - E_{eq}| = |E - (E_0 - 0.059 \cdot pH)| \tag{4.3}$$

As shown Fig. 10, the diffusion coefficient estimated is completely independent of the overpotential (thus polarisation is applied) and environments investigated. The mean value of this material is close to 4.12·$10^{-10}\frac{m^2}{s}$, consistent with literature on similar steels [36] and similar environmental conditions [37].

The estimate of diffusion coefficient reflects only the contribution of diffusible hydrogen at room temperature in these experimental conditions (apparent diffusion coefficient). During the discharging step, only diffusible hydrogen can diffuse from the sample due to the experimental conditions used in this study. Anodic polarisation ensures that the surface hydrogen concentration remains zero throughout the discharging process. Maintaining room temperature during testing allows the interaction between diffusion and trapping phenomena to be minimised. The hydrogen that is trapped inside the irreversible traps during the charging phase is not released during discharge, and therefore does not participate in the diffusion process. In general, the trapping and detrapping activation energies that alter the flow of hydrogen depend in the first instance on temperature. The energy peaks required to activate these phenomena and induce observable changes in the flow mechanisms are located at temperatures above room temperature [38,39]. This considering the same material thus with comparable microstructural conditions of vacancies, inclusions and interstitial elements that can altered the trapping phenomena [40–42]. In this way, it is possible to control diffusion conditions in three-dimensional flux under Fick's second law and to investigate the apparent diffusion coefficients. The latter must be dependent only on the material and independent of the applied polarisation and testing environment. Therefore, the initial hydrogen concentration estimated using this method indicates the solubility of diffusible hydrogen (hydrogen uptake) in this specific material and in certain experimental conditions. Specifically, the initial hydrogen concentration is strongly dependent on overpotential, and increased polarisation increases the initial hydrogen concentration in all environments tested, as shown in Fig. 11. Changing the pH value changes the equilibrium potential during charging polarisation, as indicated in Equation (4.3), even if the actual applied overpotential is altered by the formation of a local alkalinisation layer at the cathode. This effect is contrasted with the buffering property of carbonate-bicarbonate solution. About the sodium hydroxide solution, the high pH value presents an elevated quantity of OH^- ions that contrasts the H^+ formation, while for the carbonate–bicarbonate solution at pH 10, the buffering capacity that counteracts the cathode alkalinisation must be considered. In all cases, the interpretation lines do not pass through zero because of the persistent mass diffusion layer on the sample surface caused by the alkalinisation reaction.

Through the optimisation presented in this work, it is possible to estimate the apparent diffusion and solubility of hydrogen, even in complex geometries or situations in which it is not feasible to extract a tiny plate for a traditional permeation test system. There are no constraints regarding thickness or shape; the only experimental requirement is to guarantee the homogeneous electric field distribution surrounding the sample. It is sufficient to simulate the studied geometry using software (current software capabilities can handle this well), build a characteristic model curve, and use the proposed interpolation method. Moreover, this approach provides possibilities to estimate the diffusion coefficient and hydrogen uptake, and the elapsed time between the end of charging and the initial discharging step is not negligible. Thus, in each case, when it is impossible to make a discharging step immediately (e.g. after gaseous charging in autoclave or in post-charging tensile tests), this approach can be used to correctly evaluate the diffusion coefficient and hydrogen uptake.

5. Conclusion

- The method described in this study uses an electrochemical monocell, which is an easy experimental setup.
- The hydrogen uptake C_0 and diffusion coefficient D are evaluated for pipeline steel API 5L-grade X65 in different alkaline environments and cathodic charging potentials. In this case, the parameters describe the global mean value of the diffusion of hydrogen for this material.
- An optimisation numerical approach is developed to estimate the hydrogen uptake, diffusion coefficient and elapsed time using experimental data, with a target curve developed by physical simulation software.
- The hydrogen uptake C_0 is dependent on the cathodic charging potential, while the global diffusion coefficient D is determined solely by the type of material and is independent of the polarisation applied.

CRediT authorship contribution statement

Luca Gritti: Writing – original draft, Conceptualization. **Denny Coffetti:** Visualization. **Marina Cabrini:** Conceptualization. **Tommaso Pastore:** Conceptualization.

Declaration of competing interest

The authors declare that they have no known competing financial interests or personal relationships that could have appeared to influence the work reported in this paper: Luca Gritti reports was provided by Univeristy of Bergamo. If there are other authors, they declare that they have no known competing financial interests or personal relationships that could have appeared to influence the work reported in this paper.

Appendix A. Supplementary data

Supplementary data to this article can be found online at https://doi.org/10.1016/j.ijhydene.2025.02.400.

References

[1] Sofian M, Haq MB, Al Shehri D, Rahman MM, Muhammed NS. A review on hydrogen blending in gas network: insight into safety, corrosion, embrittlement, coatings and liners, and bibliometric analysis. Int J Hydrogen Energy 2024;60:867–89. https://doi.org/10.1016/j.ijhydene.2024.02.166.

[2] Zhao W, Wang W, Li S, Li X, Sun C, Sun J, Jiang W. Insights into the role of CO in inhibiting hydrogen embrittlement of X80 steel weld at different hydrogen blending ratios. Int J Hydrogen Energy 2024;50:292–302. https://doi.org/10.1016/j.ijhydene.2023.10.167.

[3] Peral LB, Díaz A, Colombo C, Alegre J, Cuesta II. Effect of electrochemical charging on the hydrogen embrittlement susceptibility of a low-alloyed tempered martensitic steel submitted to high internal pressure. Int J Hydrogen Energy 2024;63:657–67. https://doi.org/10.1016/j.ijhydene.2024.03.034.

[4] Hamed A, Posch-Peperkorn C, Maierhofer J, Beschliesser M, Fink S, Mori G. Assessing the hydrogen embrittlement susceptibility of an existing L360NB natural gas pipeline steel for 100 % hydrogen transport. Corros Sci 2025;244. https://doi.org/10.1016/j.corsci.2024.112648.

[5] Guedes D, Cupertino Malheiros L, Oudriss A, Cohendoz S, Bouhattate J, Creus J, Thébault F, Piette M, Feaugas X. The role of plasticity and hydrogen flux in the fracture of a tempered martensitic steel: a new design of mechanical test until fracture to separate the influence of mobile from deeply trapped hydrogen. Acta Mater 2020;186:133–48. https://doi.org/10.1016/j.actamat.2019.12.045.

[6] J.H. Sir William, On some remarkable changes produced in iron and steel by the action of hydrogen and acids, Nature 11 (1875) 393–393. https://royalsocietypublishing.org/.

[7] Oudriss A, Fleurentin A, Courlit G, Conforto E, Berziou C, Rébéré C, Cohendoz S, Sobrino JM, Creus J, Feaugas X. Consequence of the diffusive hydrogen contents on tensile properties of martensitic steel during the desorption at room temperature. Mater Sci Eng, A 2014;598:420–8. https://doi.org/10.1016/j.msea.2014.01.039.

[8] Thomas RLS, Scully JR, Gangloff RP. Internal hydrogen embrittlement of ultrahigh-strength AERMET 100 steel. Metall Mater Trans 2003;34:327–44. https://doi.org/10.1007/s11661-003-0334-3.

[9] Hagen AB, Nyhus B, Gerhardt MR, Musinoi Hagen CH, Stenerud G, Alvaro A, Mainçon P, Olden V. Experimental determination of equivalent hydrogen gas pressure from electrochemical hydrogen charging. Int J Hydrogen Energy 2024;82:1146–56. https://doi.org/10.1016/j.ijhydene.2024.02.117.

[10] Peng Z, Cao C, Huang F, Wang L, Xue Z, Liu J. Effect of slow strain rates on the hydrogen migration and different crack propagation modes in pipeline steel. Steel Res Int 2023;94. https://doi.org/10.1002/srin.202300070.

[11] Entezari E, Velázquez González JL, Rivas López D, Beltrán Zúñiga MA, Jack TA, Szpunar J. Experimental study on hydrogen embrittlement behavior of X80 and X70 pipeline steels evaluated by hydrogen permeation and slow strain rate tensile tests. J Fail Anal Prev 2024. https://doi.org/10.1007/s11668-024-02042-1.

[12] Wang C, Zhang J, Liu C, Hu Q, Zhang R, Xu X, Yang H, Ning Y, Li Y. Study on hydrogen embrittlement susceptibility of X80 steel through in-situ gaseous hydrogen permeation and slow strain rate tensile tests. Int J Hydrogen Energy 2023;48:243–56. https://doi.org/10.1016/j.ijhydene.2022.09.228.

[13] Kim HJ, Shin G, Park J, Lee MG, Kim KJ, Yoon SC. Pre-strain and hydrogen charging effect on the plastic and fracture behavior of quenching and partitioning (Q&P) steel. Acta Mater 2024;263. https://doi.org/10.1016/j.actamat.2023.119524.

[14] Konert F, Wieder F, Nietzke J, Meinel D, Böllinghaus T, Sobol O. Evaluation of the impact of gaseous hydrogen on pipeline steels utilizing hollow specimen technique and μCT. Int J Hydrogen Energy 2024;59:874–9. https://doi.org/10.1016/j.ijhydene.2024.02.005.

[15] Yang H, Zhang H, Liu C, Wang C, Fan X, Cheng YF, Li Y. Effects of defect on the hydrogen embrittlement behavior of X80 pipeline steel in hydrogen-blended natural gas environments. Int J Hydrogen Energy 2024;58:158–73. https://doi.org/10.1016/j.ijhydene.2024.01.107.

[16] Zafra A, Harris Z, Sun C, Martínez-Pañeda E. Comparison of hydrogen diffusivities measured by electrochemical permeation and temperature-programmed desorption in cold-rolled pure iron. J Nat Gas Sci Eng 2022;98. https://doi.org/10.1016/j.jngse.2021.104365.

[17] Masato E, Daisuke H, Toshimi T. Modeling thermal desorption analysis of hydrogen in steel. ISIJ Int 2006;46:1381–7.

[18] Galindo-Nava EI, Basha BIY, Rivera-Díaz-del-Castillo PEJ. Hydrogen transport in metals: integration of permeation, thermal desorption and degassing. J Mater Sci Technol 2017;33:1433–47. https://doi.org/10.1016/j.jmst.2017.09.011.

[19] Demarez A, Hock AG, Meunier FA. Diffusion of hydrogen in mild steel. Acta Metall 1954;2:214–23. https://doi.org/10.1016/0001-6160(54)90162-5.

[20] Ovejero-García J. Hydrogen microprint technique in the study of hydrogen in steels. J Mater Sci 1985;20:2623–9. https://doi.org/10.1007/BF00556094.

[21] Poole C. Gas chromatography. Elsevier; 2021.

[22] Cupertino-Malheiros L, Duportal M, Hageman T, Zafra A, Martínez-Pañeda E. Hydrogen uptake kinetics of cathodic polarized metals in aqueous electrolytes. Corros Sci 2024;231:111959. https://doi.org/10.1016/j.corsci.2024.111959.

[23] International Standard ISO 17081. Method of measurement of hydrogen permeation and determination of hydrogen uptake and transport in metals by an electrochemical technique. 2014.

[24] International standard ASTM G148-97. Standard practice for evaluation of hydrogen uptake, permeation, and transport in metals by an electrochemical technique. 2003.

[25] Addach H, Berçot P, Rezrazi M, Takadoum J. Study of the electrochemical permeation of hydrogen in iron. Corros Sci 2009;51:263–7. https://doi.org/10.1016/j.corsci.2008.10.024.

[26] Yan M, Weng Y. Study on hydrogen absorption of pipeline steel under cathodic charging. Corros Sci 2006;48:432–44. https://doi.org/10.1016/J.CORSCI.2005.01.011.

[27] Mckibben R, Sharp RM, Harrington DA, Pound BG, Wright GA. A potentiostatic double-step method for measuring hydrogen atom diffusion and trapping in metal electrodes-I. Theory 1987.

[28] Pound BG, Wright GA, Sharp RM. A potentiostatic double-step method for measuring hydrogen atom diffusion and trapping in metal electrodes-II. Experientia (Basel) 1987.

[29] Parkins RN, Zhou S. The stress corrosion cracking of C-Mn steel in CO2-HCO3 −CO32 − solutions. II: electrochemical and other data. Corros Sci 1997;39:175–91. https://doi.org/10.1016/S0010-938X(97)89248-7.

[30] Peral LB, Díaz A, Alegre JM, Cuesta II. Hydrogen uptake and diffusion kinetics in a quenched and tempered low carbon steel: experimental and numerical study. Int J Hydrogen Energy 2023;48:35347–65. https://doi.org/10.1016/j.ijhydene.2023.05.286.

[31] Li X, Ma X, Zhang J, Akiyama E, Wang Y, Song X. Review of hydrogen embrittlement in metals: hydrogen diffusion, hydrogen characterization, hydrogen embrittlement mechanism and prevention. Acta Metall Sin 2020;33:759–73. https://doi.org/10.1007/s40195-020-01039-7.

[32] Trasatti S. ELECTROCHEMICAL THEORY | hydrogen evolution. 2009.

[33] Luca G, Denny C, Marina C, Tommaso P. Data in brief: experimental data supporting solubility model. Data Brief 2025. https://doi.org/10.17632/c239nmw6dp.1.

[34] Gritti L, Coffetti D, Cabrini M, Pastore T. Data in brief: experimental data supporting solubility model. Data.Mendelay.Com 2025.

[35] Bockris J, Azzam A. The kinetics of the hydrogen evolution reaction at high current densities. Trans Faraday Soc 1952;48:145–60.

[36] Thomas A, Szpunar JA. Hydrogen diffusion and trapping in X70 pipeline steel. Int J Hydrogen Energy 2020;45:2390–404. https://doi.org/10.1016/j.ijhydene.2019.11.096.

[37] Fallahmohammadi E, Bolzoni F, Lazzari L. Measurement of lattice and apparent diffusion coefficient of hydrogen in X65 and F22 pipeline steels. Int J Hydrogen Energy 2013;38:2531–43. https://doi.org/10.1016/j.ijhydene.2012.11.059.

[38] Hurley C, Martin F, Marchetti L, Chêne J, Blanc C, Andrieu E. Numerical modeling of thermal desorption mass spectroscopy (TDS) for the study of hydrogen diffusion and trapping interactions in metals. Int J Hydrogen Energy 2015;40:3402–14. https://doi.org/10.1016/j.ijhydene.2015.01.001.

[39] Wallaert E, Depover T, Arafin M, Verbeken K. Thermal desorption spectroscopy evaluation of the hydrogen-trapping capacity of NbC and NbN precipitates. Metall Mater Trans A Phys Metall Mater Sci 2014;45:2412–20. https://doi.org/10.1007/s11661-013-2181-1.

[40] Park GT, Koh SU, Jung HG, Kim KY. Effect of microstructure on the hydrogen trapping efficiency and hydrogen induced cracking of linepipe steel. Corros Sci 2008;50:1865–71. https://doi.org/10.1016/j.corsci.2008.03.007.

[41] Chen YS, Huang C, Liu PY, Yen HW, Niu R, Burr P, Moore KL, Martínez-Pañeda E, Atrens A, Cairney JM. Hydrogen trapping and embrittlement in metals – a review. Int J Hydrogen Energy 2024. https://doi.org/10.1016/j.ijhydene.2024.04.076.

[42] Koren E, Yamabe J, Lu X, Hagen CMH, Wang D, Johnsen R. Hydrogen diffusivity in X65 pipeline steel: desorption and permeation studies. Int J Hydrogen Energy 2024;61:1157–69. https://doi.org/10.1016/j.ijhydene.2024.03.027.